




Article

WRF Parameterizations of Short-Term Solar Radiation Forecasts for Cold Fronts in Central and Eastern Europe

Michał Mierzwiak , Krzysztof Kroszczyński  and Andrzej Araszkievicz * 

Faculty of Civil Engineering and Geodesy, Military University of Technology, gen. S. Kaliskiego 2, 00-908 Warsaw, Poland; michal.mierzwiak@wat.edu.pl (M.M.); krzysztof.kroszczyński@wat.edu.pl (K.K.)

* Correspondence: andrzej.araszkievicz@wat.edu.pl

Abstract: The solar power industry is a rapidly growing sector of renewable energy, and it is crucial that the available energy is accurately forecast. Using numerical weather prediction models, we can forecast the global horizontal irradiance on which the amount of energy produced by photovoltaic systems depends. This study presents the forecast effects for one of the most challenging weather conditions in modelling, occurring in central and eastern Europe. The dates of the synoptic situations were selected from 2021 and 2022. Simulations were carried out for 18 days with a cold front and, in order to verify the model configuration, for 2 days with a warm front, 2 days with an occlusion front and 2 days with a high pressure situation. Overall, 24 forecasts were made for each of the three parameterizations of the Weather Research and Forecasting model. The data were compared with the values measured in situ at the station performing the actinometric measurements belonging to Germany's National Meteorological Service. This paper presents the spatial distribution of the global horizontal irradiance parameters for several terms to explain the differences between the results of the different simulations.

Keywords: solar irradiance; renewable energy sources; Weather Research and Forecasting model; photovoltaics; cold fronts



Citation: Mierzwiak, M.; Kroszczyński, K.; Araszkievicz, A. WRF Parameterizations of Short-Term Solar Radiation Forecasts for Cold Fronts in Central and Eastern Europe. *Energies* **2023**, *16*, 5136. <https://doi.org/10.3390/en16135136>

Academic Editors: John Boland and Ignacio Mauleón

Received: 31 May 2023

Revised: 22 June 2023

Accepted: 30 June 2023

Published: 3 July 2023



Copyright: © 2023 by the authors. Licensee MDPI, Basel, Switzerland. This article is an open access article distributed under the terms and conditions of the Creative Commons Attribution (CC BY) license (<https://creativecommons.org/licenses/by/4.0/>).

1. Introduction

Central and eastern Europe (CEE) have a strong, growing market for renewable energy sources (RES), due to the energy transition implemented as part of European Union (EU) efforts over the past few decades. In particular, of significant interest is the solar energy industry, especially photovoltaics (PV). The significant and steadily growing share of its electricity production [1] arises from the characteristics of this type of installation. Solar energy systems can be used as grid-connected elements or as independent sources of energy. The power produced from these systems results from the number of modules used, and is also adapted to the user's needs. The place of installation depends on an area's conditions—the panels can be installed on buildings or on independent supporting structures.

The CEE region is currently a rapidly growing PV market, despite the geographical and meteorological conditions not being ideal for solar energy systems. The unfavorable conditions are caused by the temperate latitudes of the northern hemisphere (this refers to the angle of incidence of the sun's rays) and active cyclogenesis, resulting in dynamically changing weather conditions and, especially, a significant cloud cover [2]. Economic growth has resulted in an increase in overall wealth, as well as a change in thinking about key issues for society, such as the environment and its protection. An example of a change in mentality, both of individual citizens and society as a whole, is the growing interest in renewable energy sources, recycling and the use of energy-efficient technologies, both in industry and in everyday life [3,4]. This leads to changes in important sectors of industry, such as the energy sector [5]. The continuous development of technology results in an ever-increasing amount of energy generated by the RES sector [6]. The most dynamically

growing renewable energy industry sector is solar energy, both for its conversion directly into electricity (photovoltaics) and for its transformation into thermal energy [7].

The current situation in the CEE region (an energy crisis caused by armed conflict), makes it clear how reliant citizens are on energy supply. The interruption of the fossil fuel supply chain has led to significant changes in the functioning of the European Union market. There is now an increased emphasis on the diversification of energy sources [8], as well as the continued development of the RES sector, which would guarantee energy production, independent of the availability of fossil fuel. Until recently, one of the main arguments for the development of the renewable energy industry was the reduction of pollutant emissions (primarily greenhouse gases), but the priorities have now changed. The main goal is to maintain the capacity to produce electricity, which will ensure energy security for the citizens of the CEE region as well as the entire EU [9]. The region is in the process of developing the existing or planned projects for new RES installations, especially those related to solar energy. New solar farms of various sizes or smaller solar facilities located in private households are constantly being built [10]. Investments in public utility infrastructure (offices, hospitals and schools, etc.) which, as a consequence of emission-free facilities obtaining heat or electricity from renewable sources, are becoming increasingly popular, are moving closer to achieving climate neutrality (by 2050), which is currently a priority in all strategies of the EU planning bodies [11,12].

The increasing share of energy coming from the RES sector necessitates the adaptation of the existing electricity infrastructure, changing the way energy is managed and distributed. One of the key issues is the ability to forecast production volumes, especially of electricity from renewable energy sources, including solar radiation. Knowing the future volume of this resource is very important for the power sector, primarily in terms of optimized management of the electricity grid. In regions characterized by favorable solar conditions where weather conditions are predictable and dominated by extended high-pressure systems with cloudless weather (latitudes around the tropics, the Middle East [13], North Africa, the Iberian Peninsula [14] and the Balkan Peninsula [15,16]), forecasting the amount of solar radiation reaching the Earth's surface is not as complex and difficult as it is in central and eastern Europe.

Numerical Weather Prediction (NWP) models used for the prediction of atmospheric conditions perform admirably in high pressure situations (for forecasts of solar conditions—global horizontal irradiance—Pearson's correlation against data obtained from in situ measurements is characterized by values well above 0.9) [17,18]. One of these models, the Weather Research and Forecasting model (WRF), is used to forecast many meteorological elements at different spatial scales for predictions of different lengths [19,20]. The main difficulties for forecasts with a high level of agreement with measured data are the question of the model parameterization used, the geographic static data (a type of data describing terrain and type of land cover, etc.), the type of input data, the forecast duration and several other factors (e.g., the model version and the resolution of output data or grid resolution, etc.) [21]. The models perform much worse in areas of higher latitudes. Studies in Sweden and Finland have assessed the feasibility of using NWP to forecast solar conditions in northern Europe. The results of the ensemble prediction system simulations, using meteorological cooperation on operational numeric weather prediction, were compared with other data sources, such as the satellite-based Solis–Heliosat model. The results showed that the NWP model used had satisfactory simulation results for the Fennoscandia region, although it was characterized by an underestimation of irradiance. The comparison was made for a 6 week period covering mid-July and August—the warmest period of the year with the longest days [22]. During this period, there is a polar day (a day lasting 24 h, also known as the midnight sun) in the north of the region and a prevailing contribution of clear days caused by the orographic barrier (Scandinavian Mountains), known as the rain shadow effect [23]. Research was also conducted to compare the results of simulated global horizontal irradiance (GHI) obtained by several different models in several regions—the U.S.A, Canada and Europe (Germany, Spain, Austria and Switzerland).

Researchers [24] compared the Global Environmental Multiscale Model (GEM), the High Resolution Limited Area Model (HIRLAM) and the Mesoscale Atmospheric Simulation System (MASS). The results showed that the WRF performed best compared to the other mesoscale models; however, the simulations covered 7 days, but did not specify the synoptic conditions for which the predictions were made. Another study [17] analyzed forecasts of solar conditions for north-eastern Germany for the most unfavorable synoptic situations (days with moving atmospheric fronts), which represent a significant proportion of the annual weather conditions. The study showed that the WRF model used had good results for days with warm fronts or occluded fronts. Notably high correlation coefficients were achieved for the days with high pressure situations. In contrast, the WRF model performed worst for the days with cold fronts [25]. The model's results for several configurations were compared with the measured data at Germany's National Meteorological Service (later termed DWD—Deutscher Wetterdienst) stations and the ERA5 reanalysis.

The geographical location of central and eastern Europe is a major factor determining the complex atmospheric conditions, which are subject to dynamic changes in both time and space. Influences of the Atlantic Ocean and the Eurasian continent clash over Europe, which means that the western part of Europe is predominantly influenced by the Atlantic, while the eastern part is mainly influenced by the continent's interior (Eurasia). Central and eastern Europe are located in the zone that mixes both influences (the climate varieties are maritime and continental) [26]; hence, the atmospheric conditions prevailing in this part of the continent are extremely complicated and difficult to forecast. The contribution of air masses from the Arctic and Atlantic oceans to meteorological and, in the longer term, climatic conditions is significant, as described in [27,28]. The difficulties associated with predicting the amount of solar radiation reaching the Earth's surface under conditions of dynamically changing atmospheric humidity result in a significant underestimation of the volume of energy that can be produced from solar installations, especially in the summer and winter seasons. An improved forecast of the solar conditions would significantly enhance the management of energy resources during periods of high electricity demand.

Studies on atmospheric humidity show that it has a very important influence, not only in terms of its contribution to the formation of water vapor condensation products [29], but also playing a very important role in the context of the radiation process. It directly affects the scattering, reflection and absorption of short-wave radiation from the sun, which sometimes significantly modifies the amount of solar radiation reaching the Earth's surface [30,31]. The effect of the water vapor on the amount of radiation is also evident in the case of clear sky conditions [32]. Decreasing the radiation reaching the Earth's surface primarily affects the Earth's radiation balance, as well as translating into the functioning of the solar renewable energy sector. Studies confirm that the water vapor content is an important element affecting the amount of energy reaching the Earth's surface, hence the analysis of the magnitude of this indicator and the possibility that its forecasting could contribute to improving the quality of forecasting solar conditions [29]. Increasingly, non-meteorological measurements, including observations from global navigation satellite systems (GNSS), are being used in the study of water vapor distribution and changes. These analyses have confirmed their applicability in climate research [33,34]. Dense networks of GNSS stations allow the collection of data with high spatial and temporal resolution, which have not been provided by the previous measurement methods (e.g., aerial surveys). The analysis of longer time series allows the detailed observation of changes occurring in both large (covering Europe, the Middle East and northern Africa) [35] and small (involving Svalbard) [36] areas. Studies of central and eastern Europe, based on precipitable water (PW) extracted from GNSS data, have shown that, in recent years, the magnitude of this parameter varies from year to year and from season to season. The results of the studies show differences in the magnitude of precipitation water directly related to geographical location and seasonal variations and trends [26]. Due to ongoing climate change on a global as well as local scale, a further increase in PW values over the CEE region directly linked to a systematic increase in temperature is expected.

A characteristic feature of central and eastern Europe is the numerous atmospheric fronts moving over it throughout the year. These mainly come from the western sector, bringing a change in atmospheric conditions, most often transporting polar-maritime air masses that are rich in moisture, which bring cooling and precipitation in summer, while in autumn and winter they are associated with warming and precipitation. The forecasting effectiveness for synoptic situations associated with moving atmospheric fronts, especially cold fronts, is much worse than for high pressure situations, as previous analyses have shown [17].

The aim of the present study was to simulate the global horizontal irradiance. North-eastern Germany was chosen as the study area. The analyses were carried out using the WRF model. The most challenging aspect was the prediction of solar conditions for days with cold fronts. The study paid particular attention to the magnitude of global horizontal irradiance (GHI). This plays an important role in the renewable energy sector related to solar installations. This study is a continuation of the research on forecasting solar conditions for central and eastern Europe and addresses short-term forecasts of the GHI parameter. It is a starting point for further work on medium-term forecasts of solar conditions. The main goal of the study is to assess the possibility of forecasting global horizontal irradiance, for dynamic atmospheric conditions that are cold fronts with accompanying hazardous phenomena (thunderstorms and intense precipitation, etc.), which are characteristic features of weather for the analyzed region. Different parameterizations of the WRF model were analyzed to identify which would perform better in forecasting solar conditions for cold fronts in CEE.

In the present study, the authors decided to evaluate the effect of activating the cumulus parameterization (for the analyzed CEE area) on the solar conditions' forecast (GHI) for a domain with a spatial resolution of 3 km. In the default (recommended) configuration, it is deactivated. Similar experiments have been carried out in the United States of America [37] showing that the domains with the largest spatial resolutions (3 km and 1 km) had the best results relative to those with coarser ones.

2. Materials and Methods

The solar forecasting studies were carried out in eastern Germany. The study was conducted during dynamically changing weather conditions associated with moving cold fronts. Eighteen dates from the 2021–2022 season were selected, for which WRF model simulations were performed and verified with data from ground stations. The detailed methods of the study are described in the following subsections.

2.1. Region of Analysis

The region under study is situated between 50.2° and 52.7° north latitude and between 10.7° and 15.2° east longitude. This is an area that is characterized by non-optimal solar conditions, mainly due to the complex weather conditions prevailing in the temperate latitudes (large differences in the length of day and night during the year, active cyclogenesis responsible for, among other things, large, time-varying cloud cover, etc.). Despite the existing barriers, mainly due to its geographical location, the area is characterized by significant potential due to the terrain (lowland and hilly areas). German policy focuses on the further intensive development of RES, including the solar sector, which is the fastest growing RES industry [38]. One example is the construction of a floating photovoltaic power plant, which will be located on the Cottbus Ostsee (created after the flooding of an opencast lignite mine). There are plans to develop more facilities of this type in the Lusatia region [39]. In this context, forecasting solar conditions for the region gains additional importance [40].

The central and northern parts of the analyzed region (Figure 1) are located within the central European lowlands—Leipzig (central German lowlands), Potsdam, Lindenberg (south Baltic lakes). The southern part is the foothills of the Ore Mountains and the Sudeten Mountains (Dresden, Chemnitz and Goerlitz, respectively). The natural landscapes of the

first three locations are denudation plains with moraines, eskers and kames, separated by river valleys of considerable widths and irregular terrain depressions. The next three stations are located at the foothills of the Bohemian Massif (whose north-eastern and north-western fragments are the Sudeten and Ore Mountains [41,42]).

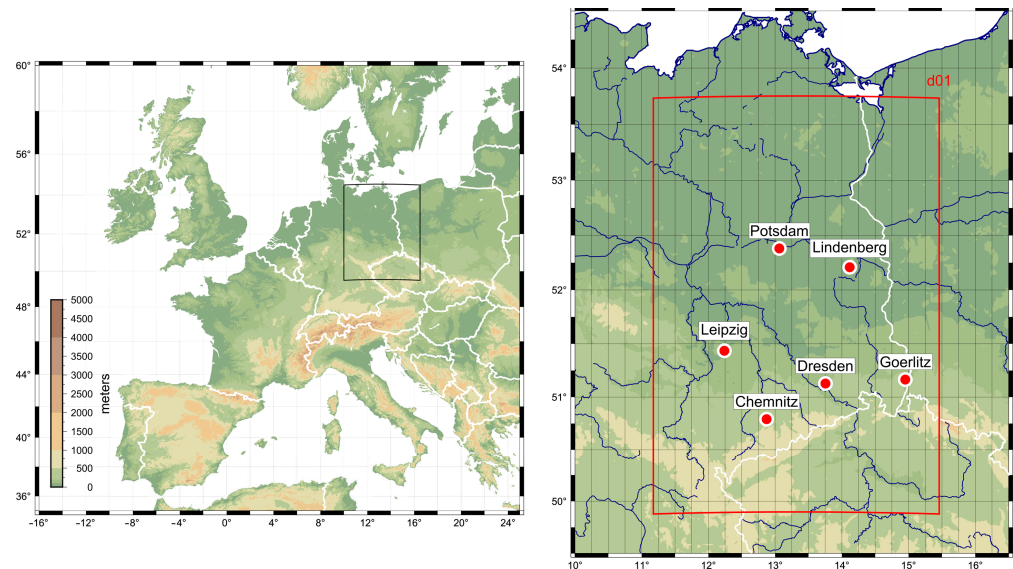


Figure 1. The area selected for analysis (on the left). Domains d01 and the location of the DWD stations are marked on the right.

2.2. Synoptic Situations

For the purpose of the study, the period from the beginning of April 2021 to the end of March 2022 was analyzed in terms of the frequency of atmospheric fronts over the area of interest. Synoptic maps prepared by the Institute of Meteorology and Water Management—National Research Institute [43] were used for the analyses. Due to the subject of the study, the situations in which the front was located and thus formed the weather over the analyzed region during the day were taken into account. In the aforementioned period, 87 atmospheric fronts meeting the above criteria were recorded, including 17 warm fronts, 34 cold fronts and 36 occluded fronts (representing 19.5%, 39.1% and 41.4%, respectively). The above analysis confirmed the results of studies with longer observation periods [44], where the frequency of fronts was similar. Days with cold fronts (moving through the day) account for about 10% of the calendar year. Together with warm and occluded fronts and their accompanying cloud cover, they are responsible for a significant worsening of solar conditions in the CEE region for more than 100 days per year. Analysis of the 12 months shows a characteristic regularity. Two periods of increased frontal activity are visible: spring–summer and autumn–winter. An analysis of the 12 months shows a characteristic regularity. Figure 2 shows the number of atmospheric fronts by type recorded in a given month that moved over the analyzed area during the day (based on the synoptic maps from 12:00 UTC [43]).

Figure 2 shows the periods during the year with increased overall activity of atmospheric fronts (summer: July–August and autumn–winter: October–December), separated by months with a smaller number of fronts (on average, there are 7.25 atmospheric fronts per month). The fact that the maxima in the frequency of occurrence of cold fronts take place in both the months with the highest amount of solar radiation reaching the Earth’s surface (June–July) and the lowest (November–December) is important from the point of view of its forecasting. The summer season accounts for the highest value of electricity generated by photovoltaic installations, whereas the winter season is characterized by a noticeably smaller supply of solar radiation. In both cases, any value is important.

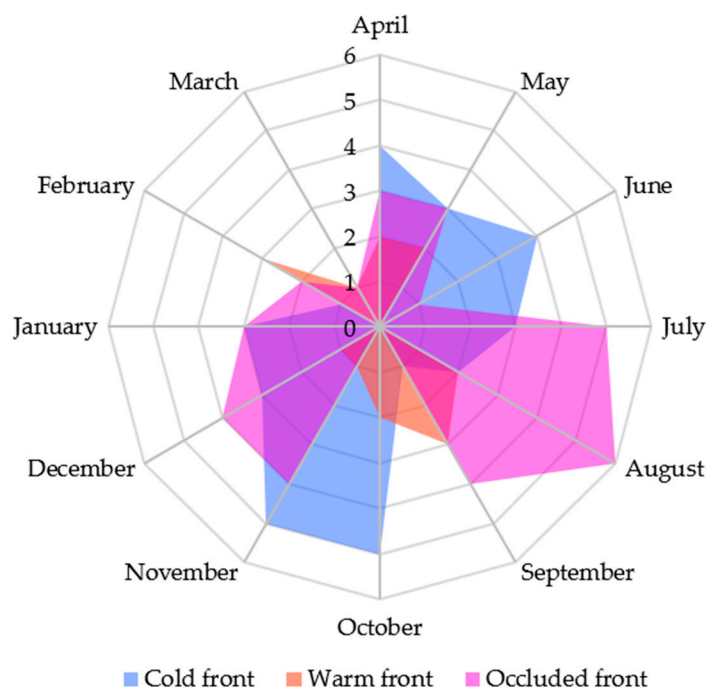


Figure 2. Frequency of atmospheric fronts during the year (April 2021–March 2022) over the study area (12:00 UTC).

Based on the analysis of synoptic situations, 18 dates were selected to carry out a solar forecast. This represents more than half of the cases ($\approx 53\%$) of the recorded cold fronts during the considered period (April 2021–March 2022). Twelve of the fronts considered are cold fronts, while the remaining six are waving fronts [45]. Additionally, in five cases (Table 1) a convergence line was formed ahead of the frontal boundary. It formed along the horizontal convergence of air streams and, in the cases analyzed, was located in the warm sector. This line is associated with the formation of convective clouds (e.g., cumulus cloud—Cu) [46,47].

Table 1. A summary of terms analyzed by synoptic situation.

Cold Fronts		
1 April 2021 (WF + CL)	7 July 2021 (WF + CL)	1 November 2021 (WF)
5 April 2021	28 July 2021 (CL)	7 November 2021
29 April 2021 (WF)	22 August 2021 (CL)	13 November 2021
25 May 2021	11 October 2021 (WF)	23 November 2021
12 June 2021 (CL)	12 October 2021	16 December 2021
15 June 2021	15 October 2021 (WF)	17 January 2022

WF—waving front; CL—convergence line.

2.3. WRF Parameterization

The WRF model simulations were carried out for the above area in the d01 domain with a horizontal grid spacing of 3 km (Figure 1). Inputs of the initial conditions and lateral boundary conditions from the Global Forecast System model were used for the forecasts, with a resolution of 0.25 degrees and a temporal resolution of 3 h [48]. Each of the 24 simulations was run 12 h before the day of analysis and ended at 00:00 the following day (the start was 12:00 UTC of the day before the date under analysis, at 00:00 UTC of the day under consideration—end of simulation), with a one-hourly output. The research conducted showed that forecasts run with such a spin-up time of 12 h guarantee the best forecasting results in the analyzed case (compared to 3, 6, 9, or 15 h ahead). Forecasts from 03:00 to 21:00 on a given day were taken into account for the analyses. This is the time of

day when the sun's rays directly reach the Earth's surface in the cases analyzed. Predictions were made on version 4.3.3 of the WRF model. The following model configuration was used in the study: the Thompson microphysics scheme [49], the boundary layer represented by the Mellor–Yamada Nakanishi and Niino scheme [50–52], the shortwave radiative process characterized by the rapid radiative transfer model for general circulation models (RRTMG) [53] (configuration settings to enable the WRF-Solar option [54,55]), the surface layer improved MM5 scheme [56], land surface—the Unified Noah Land Surface Model and the shallow cumulus was characterized by the Deng scheme [55,57,58]. Simulations were performed for three configurations. The default configuration (C-ref) represents the basic parameterization of the WRF model, activating the WRF-Solar module [55,59]. This configuration was treated as the reference configuration. The next two configurations, C1 and C2, represent a modification of the defaults, additionally including a cumulus parameterization (the Kain–Fritsch scheme). In configuration C1, cloud overlapping was additionally used [19]. In configuration C2, the kfeta_trigger was used [21]. The initial and boundary meteorological conditions depend on the input data used—the GFS [48]. A summary of the three model configurations analyzed is provided in Table 2.

Table 2. Summary of the main configuration parameters of the WRF model.

Model	WRF Configurations		
	C-ref	C1	C2
Horizontal resolution		d01: 3000 [m]	
Vertical resolution		45	
Microphysics		Thompson Scheme	
Planetary boundary layer		Mellor–Yamada Nakanishi Niino (MYNN)	
Longwave radiation scheme		RRTMG	
Shortwave radiation scheme		RRTMG	
Land surface options		Unified Noah Land Surface Model	
Surface layer options		Revised MM5 Scheme	
Cumulus physics	-	Kain–Fritsch (new Eta) scheme	Kain–Fritsch (new Eta) scheme
Additional options	-	cldovrlp = 3 (cloud overlapping option for RRTMG scheme; 3—maximum value)	kfeta_trigger = 3 (RH—dependent additional perturbation)

2.4. Ground Data and Errors

The WRF GHI forecasts were compared with the values measured at meteorological stations performing actinometric measurements, operating within the DWD network. The stations are located in Potsdam, Lindenberg, Dresden, Leipzig, Goerlitz and Chemnitz [60,61] (Table 3 and Figure 1). Five of the analyzed stations are located in the range of the climate zone with code Dfb, according to the Koeppen–Geiger climate classification (cold climate and no dry season, with warm summers). The area around Dresden is classified as a climate with code Cfb (temperate climate and no dry season, with warm summers).

The following metrics were used to compare the results of the forecasts with the in situ data: Pearson's correlation coefficient, root mean square error (RMSE), mean absolute error (MAE) and mean bias error (MBE) [62]. These statistics are the most commonly used to compare model data and observed data. Taken together, they convey a comprehensive picture of the compiled sets [63].

Table 3. The characteristics of DWD stations.

Station Name	Geographical Coordinates (°)		Height above Sea Level (m)
	N	E	
Potsdam	52.3812	13.0622	81
Lindenberg	52.2085	14.1180	98
Leipzig	51.4347	12.2396	131
Dresden	51.1278	13.7543	227
Goerlitz	51.1621	14.9506	238
Chemnitz	50.7913	12.8720	416

3. Results from Cold Front Situations

The analysis of the results of the forecasts of 18 situations with a cold front is presented in the following subsections dealing with individual statistics. The results have been grouped with respect to the indicators describing the data and further divided into two sections: the first presents a comparison with respect to the dates, and the second with respect to individual stations.

3.1. Pearson’s Correlation Coefficient

The analyzed situations with cold fronts were compared in terms of correlation (Pearson’s coefficient) for three configurations of the WRF model—C1, C-ref and C2. This is one of the basic indicators for comparing model simulation results with observed data [63]. The coefficients are shown in Figure 3. In most terms, the differences are not significant. However, in a few situations (including 25 May 2021, 22 August 2021 and 11 October 2021), significant discrepancies are apparent.

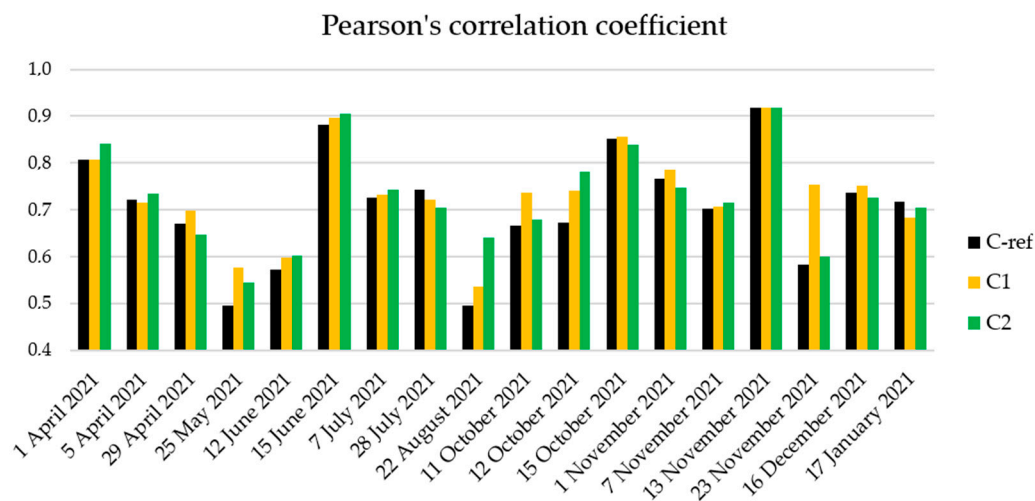


Figure 3. A comparison of Pearson’s correlation coefficient [-] for 18 cold front dates.

Figure 3 shows that the largest differences in Pearson’s correlation coefficients between configurations, exceeding the value of 0.1, occur on the 22 August 2021 (0.14), 12 October 2021 (0.11) and 23 November 2021 (0.17). The maximum value of Pearson’s coefficient for days with cold fronts was the same for all configurations (0.92), while the smallest value was characterized by the default configuration (0.49). For C1 and C2, it was 0.54.

In the case of the analysis of the distribution of Pearson’s correlation coefficients carried out for individual stations (Table 4) during the days when the weather was shaped under the influence of the conditions associated with the moving cold front, slightly higher values were characterized by the C1 and C2 (0.78) configurations relative to the C-ref (0.76); the difference was 0.02. Only for the default configuration did the coefficient have a value below 0.7 (Lindenberg station). Among stations, the one located in Leipzig performed best

(0.85), while the smallest values of Pearson's coefficient (0.74) were in Lindenberg, Potsdam and Dresden. The largest differences in correlation values occurred in Lindenberg (0.09), while for the other stations, they did not exceed 0.03.

Table 4. Pearson's correlation coefficients [-] for specific DWD stations.

	Dresden	Leipzig	Potsdam	Lindenberg	Goerlitz	Chemnitz
C-ref	0.74	0.85	0.74	0.69	0.74	0.80
C1	0.74	0.87	0.73	0.78	0.75	0.79
C2	0.76	0.84	0.74	0.76	0.77	0.80

The highest correlation coefficients, equal to or greater than 0.79, were obtained for Leipzig (C-ref: 0.85; C1: 0.84; C2: 0.87) and Chemnitz (C-ref and C1: 0.80; C2: 0.79). The worst values were obtained for the Lindenberg station, which ranged from 0.69 (C-ref) to 0.78 (C2). The largest differences in Pearson's index values between the different configurations were in the Lindenberg station (0.69–0.78). For the other stations, the differences did not exceed 0.3. The citation shows that the average values for Pearson's coefficient for the different configurations are similar, although the default configuration (C-ref) has a 0.02 lower value than the others (C1, C2).

Higher values of the correlation coefficient were characterized by dates in the cool season (average values for all configurations ranged from 0.73 to 0.77). Slightly smaller values, on the other hand, characterized the months in the warm season, from (on average) 0.68 to 0.71, depending on the configuration. In both the cool and warm seasons, the smallest average Pearson's correlation coefficients were characteristic of the default configuration (C-ref), 0.73 and 0.68, respectively.

3.2. Root Mean Square Error

The root mean square error for the analyzed cases is characterized by similar values achieved by simulations carried out for the three configurations (Table 5). The lowest RMSE values were in Leipzig and Chemnitz. In both cases, the average RMSE values (for all configurations) do not exceed 120 [$\text{W}\cdot\text{m}^{-2}$]; they are 114.32 [$\text{W}\cdot\text{m}^{-2}$] and 119.99 [$\text{W}\cdot\text{m}^{-2}$], respectively. In this comparison, Lindenberg was the worst with an average RMSE value of 134.64 [$\text{W}\cdot\text{m}^{-2}$]. Considering the RMSE values produced by each station, the best performing configuration was C1, with the smallest (average) value of 123.7 [$\text{W}\cdot\text{m}^{-2}$]. However, the differences between the various configurations were not large—the highest value was produced by C-ref (126.41 [$\text{W}\cdot\text{m}^{-2}$]).

Table 5. The root mean square error values [$\text{W}\cdot\text{m}^{-2}$] for specific DWD stations.

	Dresden	Leipzig	Potsdam	Lindenberg	Goerlitz	Chemnitz
C-ref	127.65	112.12	128.65	141.93	129.71	118.40
C1	121.63	119.05	125.01	131.82	124.29	120.40
C2	126.83	111.78	129.52	130.18	125.43	121.19

Figure 4 shows that the largest differences in RMSE are in the spring and summer months (29 April 2021, 25 May 2021, 12 June 2021 and 28 July 2021), with values above 15 [$\text{W}\cdot\text{m}^{-2}$]. During the autumn–winter season, the RMSE difference value of 15 [$\text{W}\cdot\text{m}^{-2}$] was exceeded twice: 12 October 2021 and 23 November 2021. It is clearly visible from Figure 4 that the RMSE values depend on the amount of radiation reaching the Earth's surface, reaching the highest values in the spring–summer season and the lowest in the autumn–winter season. The exceptions to this rule are the dates of 15 June 2021 and 7 July 2021, when the values of RMSE were much smaller (below 140 [$\text{W}\cdot\text{m}^{-2}$]). The average RMSE values, for dates with cold fronts, ranged from 108.5 [$\text{W}\cdot\text{m}^{-2}$] (C1) to 110.1 [$\text{W}\cdot\text{m}^{-2}$] (C-ref). At the same time, the highest RMSE values were achieved on 25 May 2021 and 12 June 2021 by the C-ref configuration, with values exceeding 200 [$\text{W}\cdot\text{m}^{-2}$] (214.6 and

206.5 [$\text{W}\cdot\text{m}^{-2}$], respectively). The RMSE values for all dates with moving cold fronts combined were 126.76 [$\text{W}\cdot\text{m}^{-2}$] for the default configuration (C-ref), while the values for the other configurations were C1: 123.78 [$\text{W}\cdot\text{m}^{-2}$] and C2: 124.31 [$\text{W}\cdot\text{m}^{-2}$]. The differences between the minimum RMSE values among the configurations were negligible (not exceeding 0.65 [$\text{W}\cdot\text{m}^{-2}$]), while the maximum values for the C1 and C2 configurations were similar (198.81 and 198.95 [$\text{W}\cdot\text{m}^{-2}$], respectively), and for C-ref the value was 214.58 [$\text{W}\cdot\text{m}^{-2}$].

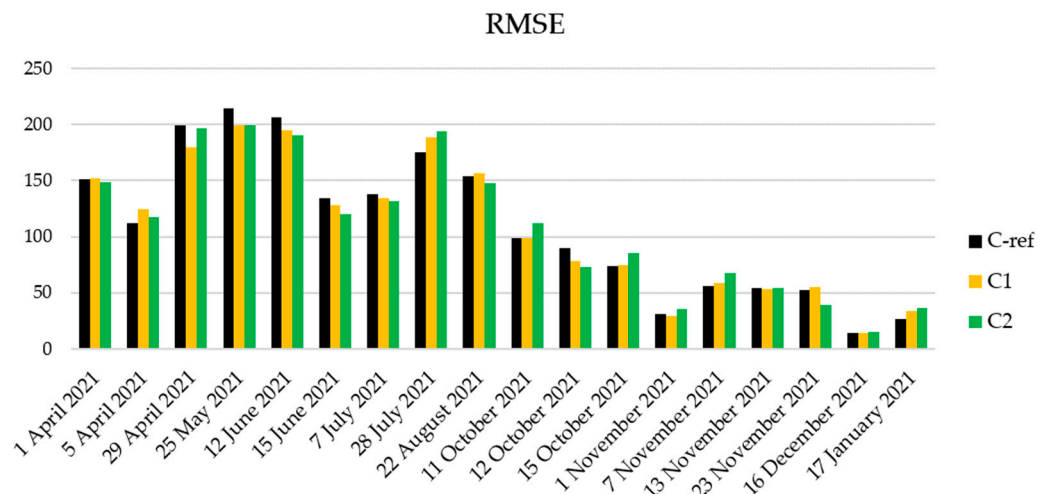


Figure 4. A comparison of RMSE [$\text{W}\cdot\text{m}^{-2}$] for 18 cold front dates.

3.3. Mean Absolute Error

The mean absolute error, in addition to having smaller values than the RMSE, is not affected by extreme values (because errors are squared before they are averaged—the RMSE gives relatively high weight to large errors). It is also widely used in the RES sector, to precisely evaluate the performance of specific parameter forecasts [63].

Table 6 shows that, in terms of the MAE values, the analyzed model configurations are characterized by similar magnitudes. The smallest MAE values characterize Chemnitz and Leipzig, and the largest values characterize the stations in Lindenberg and Potsdam.

Table 6. The mean absolute error values [$\text{W}\cdot\text{m}^{-2}$] for specific DWD stations.

	Dresden	Leipzig	Potsdam	Lindenberg	Goerlitz	Chemnitz
C-ref	69.74	64.25	71.10	75.64	68.40	61.48
C1	70.19	63.80	70.56	72.34	66.53	64.47
C2	65.32	65.77	69.07	71.26	65.89	63.74

The differences between the simulation results performed for each configuration in the case of MAE were characterized by small differences, with the smallest value achieved by C-ref (61.48 [$\text{W}\cdot\text{m}^{-2}$]) and the largest also by C-ref (75.64 [$\text{W}\cdot\text{m}^{-2}$]). The largest discrepancies between MAE values occurred for stations located in Dresden and Lindenberg (4.87 and 4.38 [$\text{W}\cdot\text{m}^{-2}$], respectively).

Similarly to the RMSE, the MAE had the highest values during the warm season, exceeding 100 [$\text{W}\cdot\text{m}^{-2}$] on 29 April 2021, 25 May 2021, 12 June 2021 and 28 July 2021 (Figure 5). The average MAE values in the autumn–winter season (November to January) reached values nearly four times smaller than those of the spring–summer season (April to August). The MAE values were very similar for the analyzed configurations, for the cool season, ranging from 27.53 [$\text{W}\cdot\text{m}^{-2}$] (C1) to 29.35 (C2), while in the warm season they ranged from 106.16 [$\text{W}\cdot\text{m}^{-2}$] (C1) to 108.68 [$\text{W}\cdot\text{m}^{-2}$] (C-ref). The largest discrepancies between the MAE values (exceeding 10 [$\text{W}\cdot\text{m}^{-2}$]), achieved by simulations performed using each configuration, occurred on 29 April 2021 (16.47 [$\text{W}\cdot\text{m}^{-2}$]), 12 June 2021 (11.23 [$\text{W}\cdot\text{m}^{-2}$])

and 28 July 2021 (12.46 [W·m⁻²]). While the differences between the minimum MAE values achieved by the different configurations were less than 0.3 [W·m⁻²], the maximum values exceeded 8.67 [W·m⁻²] (C-ref: 154.75 [W·m⁻²] and C1: 145.02 [W·m⁻²]).

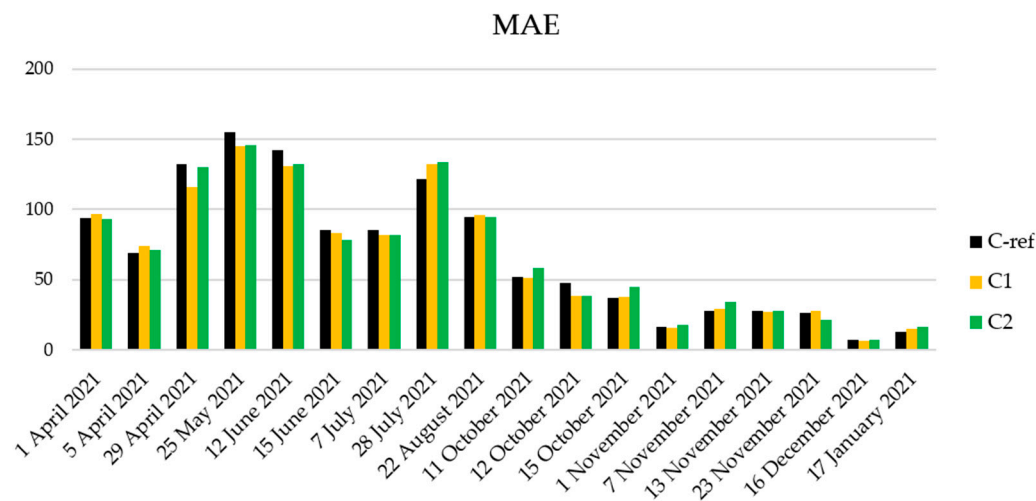


Figure 5. A comparison of the MAE values for 18 dates with cold fronts [W·m⁻²].

3.4. Mean Bias Error

The mean bias error (MBE) provides information about the nature of the average value of the model—whether the results are overestimated or underestimated. In the analyzed cases, almost all situations are slightly overestimated. Table 7 below summarizes the MBE values for each configuration characterizing the DWD stations analyzed.

Table 7. The mean bias error (MBE) values for each DWD station [W·m⁻²].

	Dresden	Leipzig	Potsdam	Lindenberg	Goerlitz	Chemnitz
C-ref	1.29	16.49	13.38	24.90	4.53	3.44
C1	5.99	27.95	17.98	36.62	5.41	9.16
C2	6.28	20.01	13.91	31.68	12.32	13.20

The above summary shows that the smallest MBE values are characterized by stations in Dresden, Goerlitz and Chemnitz, where the average, considering the results for all configurations, did not exceed 10 [W·m⁻²]. The remaining stations had much higher values of differences between the model configurations, from 15.09 [W·m⁻²] (Potsdam) to 31.06 [W·m⁻²] (Lindenberg). Dresden station had the lowest MBE values (from 1.29 [W·m⁻²] (C-ref) to 6.28 [W·m⁻²] (C1)), while Lindenberg was the worst (from 24.90 [W·m⁻²] (C-ref) to 36.62 [W·m⁻²] (C2)). For MBE values, the default configuration (C-ref) was the most favorable. Figure 6 below shows the distribution of MBE values for the three configurations for all 18 cold front dates.

Similarly to the previously analyzed errors, the cold season is characterized by lower values (from 8.77 [W·m⁻²] (C-ref) to 12.84 [W·m⁻²] (C2)) relative to the spring–summer season, in which MBE ranged from 12.57 [W·m⁻²] (C-ref) to 21.53 [W·m⁻²] (C2). On average, for dates with moving cold fronts, the default configuration had the smallest MBE values (10.67 [W·m⁻²]), while having the largest differences among the 18 dates analyzed. The absolute difference between the smallest and largest MBE values for C-ref was 126.53 [W·m⁻²], while for C1 it was 108.49 [W·m⁻²], and for C2, 117.95 [W·m⁻²]. It is interesting to note that the default configuration (C-ref) had the lowest minimum MBE value, which was 17.39 [W·m⁻²] and 22.92 [W·m⁻²] lower than the results obtained with the configurations, C2 and C1, respectively. The C-ref configuration, on the other hand, was at the same time characterized by the largest discrepancies in accepted values, from

$-66.95 [W \cdot m^{-2}]$ to $59.58 [W \cdot m^{-2}]$, resulting in an absolute difference of $126.53 [W \cdot m^{-2}]$, which is larger than the C1 configuration by $18.04 [W \cdot m^{-2}]$ and the C2 by $8.58 [W \cdot m^{-2}]$. The chart shows that the largest discrepancies between MBE values obtained through each configuration occur on 22 August 2021 and 23 November 2021. For the default configuration, the MBE values were underestimated seven times, while for the C1 and C2 configurations they were underestimated four times. Hence, it follows that the C1 and C2 configurations are more likely to overestimate the simulation results of the GHI parameter.

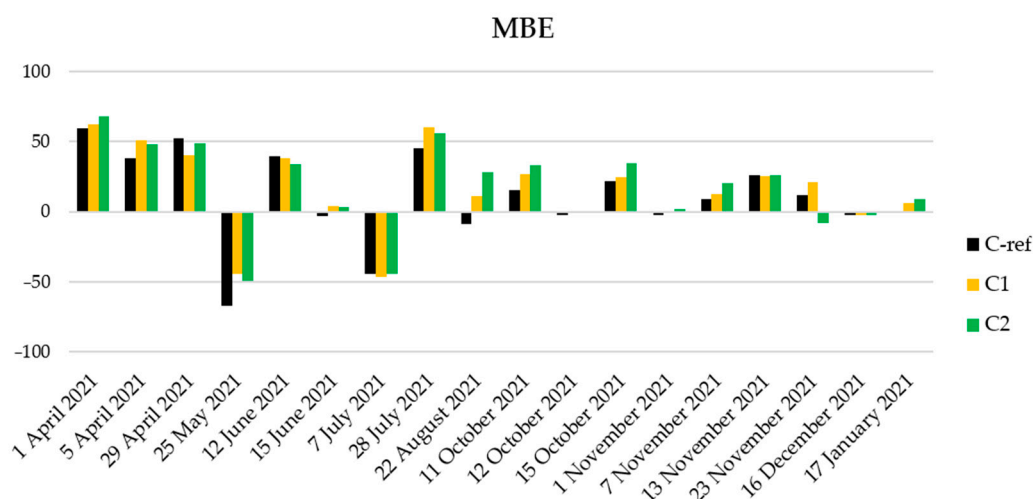


Figure 6. A comparison of MBE values for 18 dates with cold fronts [$W \cdot m^{-2}$].

The maps below (Figure 7) show the differences in daily average values of the SWDOWN parameter for the two dates, 21 May 2021 (Figure 7a) and 27 August 2021 (Figure 7b), associated with the occluded front. In the first row are the differences between the default configuration (C-ref) and C1, in the second row, C-ref and C2, the third row shows the differences between the two modified configurations (C1 and C2).

It is characteristic to take positive values of the differences between the default configuration and C1 and C2 for the summer term (27 August 2021) and negative values for 21 May 2021 (spring). In both cases, larger differences are found in the southern part of the area. Smaller values occur for differences between C-ref and C1. The differences in the values between C-ref and C2 were larger and covered a broader area. A comparison of SWDOWN values for the modified configurations (C1 and C2) highlights, especially for the southern part of the area under consideration, the significant differences between them. This is no longer as noticeable in the context of comparing the results for individual stations, when the discrepancies, for example, in the case of Pearson's correlation coefficient, did not exceed 0.02. The character of the spatial distribution and the values of the differences themselves (between C-ref and C1, and C-ref and C2) on 21 May 2021 indicates the significant influence of relief and absolute altitude. In the case of the summer date (27 August 2021), clear differences are evident in the southern part of the region, but are also found in the central part.

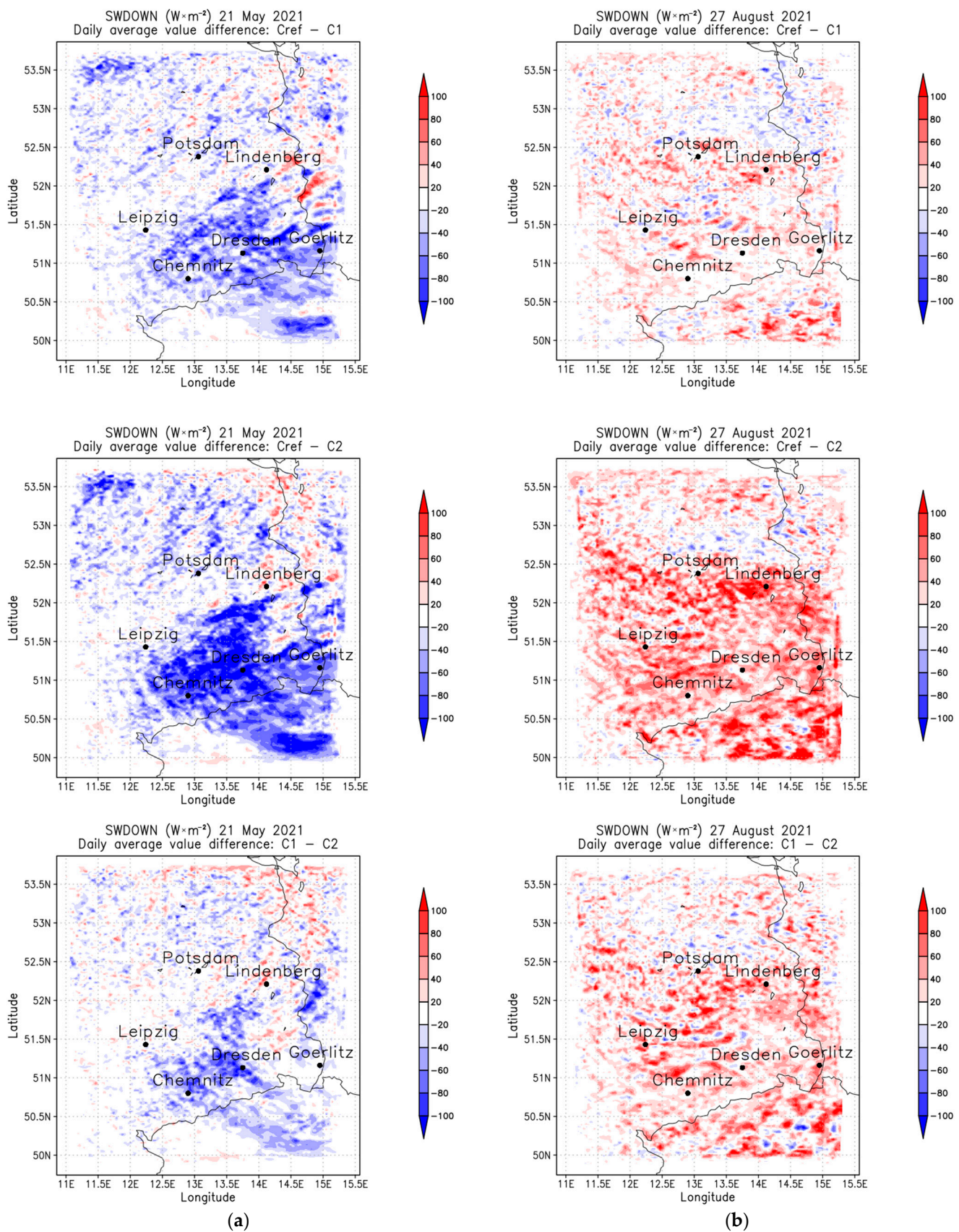


Figure 7. Maps showing average daily differences in SWDOWN values in the analysis area for dates with occluded fronts. For each date, (a) 21 May 2021 and (b) 27 August 2021, the differences between C-ref and C1, C-ref and C2, and C1 and C2, are presented.

4. Results from Non-Cold Front Cases

The verification of the presented WRF model configurations consisted of comparing data from ground stations (DWD) and data representing simulation results for six dates with different weather conditions. Two cases each were selected for the warm front, the occluded front and the high pressure situations. Similarly to the main analysis, the model data were compared with measured data from the DWD stations (Table 8).

Table 8. The summarized statistics for examined WRF configurations: Pearson’s coefficient [-], RMSE, MAE, and MBE [$W \cdot m^{-2}$].

	Pearson’s Coefficient			RMSE			MAE			MBE		
	C-ref	C1	C2	C-ref	C1	C2	C-ref	C1	C2	C-ref	C1	C2
Warm fronts												
15 April 2021	0.87	0.89	0.87	141.06	138.59	137.44	89.72	85.55	86.90	59.02	64.47	62.78
9 December 2021	0.78	0.78	0.75	27.81	31.04	41.18	12.68	14.02	18.38	9.08	11.44	16.16
Occluded fronts												
21 May 2021	0.78	0.84	0.85	167.73	144.64	138.30	110.96	91.97	89.92	-55.61	-13.48	3.42
27 August 2021	0.71	0.84	0.81	119.36	92.06	104.61	70.30	54.98	62.73	-25.88	-2.42	5.49
High pressure situations												
14 June 2021	0.96	0.96	0.96	99.70	99.70	99.68	52.38	52.38	52.32	-19.57	-19.57	-19.48
14 September 2021	0.98	0.98	0.98	49.62	49.62	49.62	33.58	33.58	33.58	-15.98	-15.98	-16.00
Overall:	0.91	0.92	0.92	105.84	100.21	102.32	58.07	54.35	56.80	10.95	17.07	18.62

The results of the analyses summarized in the Table 8 show a slight advantage of configurations including cumulus parameterization (C1 and C2) over C-ref, as is evident in Pearson’s coefficient, the RMSE and MAE. The MBE values, as in the cold front statements, reach the lowest values for the default configuration (C-ref). In each case, the model overestimated the amount of radiation reaching the Earth’s surface (GHI). Analyzing the value of Pearson’s correlation coefficient for individual dates (Figure 8), it is apparent that the default configuration achieves weaker results for dates with occluded fronts (21 May 2021 and 27 August 2021). On these days, discrepancies between correlation values range from 0.08 to 0.14, respectively. For these days, the RMSE also appeared worse for the C-ref model, by approximately 20%. For two of the terms (high pressure situations), as expected, all configurations exhibited the highest values in the set. Interestingly, both the 14 June 2021 and 14 September 2021 models were characterized by equal Pearson’s index values of each configuration (0.96 and 0.98, respectively). In the other two situations (15 April 2021 and 9 December 2021) associated with warm fronts, the discrepancies between the configurations did not exceed 0.04.

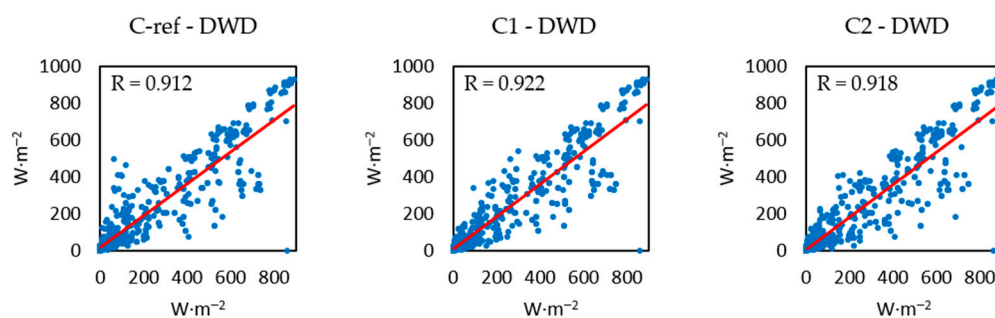


Figure 8. Scatter plots for the three parameterizations for all six dates (non-cold front cases).

Overall, all three configurations showed a very high correlation with the measured data—above 0.91 in each case (Table 8 and Figure 8), which confirms that the configurations perform well in the other remaining synoptic situations.

Table 9 shows that, in terms of Pearson's correlation coefficient, the stations located in Leipzig and Dresden performed most favorably; the average values (considering the three analyzed configurations) were 0.94 and 0.93, respectively. The worst in the comparison was the station in Chemnitz, at 0.87. When analyzed on a station-by-station basis, the configurations that included cumulus parameterization did slightly better: C1 and C2 (by 0.02 relative to C-ref). With the exception of the Chemnitz station, all the correlation values were above 0.90.

Table 9. A summary of Pearson's correlation coefficients [-] for the examined WRF configurations by station.

	Dresden	Leipzig	Potsdam	Lindenberg	Goerlitz	Chemnitz
C-ref	0.90	0.94	0.90	0.91	0.91	0.87
C1	0.94	0.95	0.91	0.92	0.93	0.88
C2	0.94	0.93	0.93	0.93	0.92	0.87

Table 10 shows the results of the comparison of RMSE values for each station for six terms, characterizing days with warm fronts, occluded fronts and high pressure conditions. The smallest values are characterized by configurations C1 and C2, which obtained similar results of 102.77 and 102.38 [$W \cdot m^{-2}$], respectively, while the default configuration was 110.85 [$W \cdot m^{-2}$]. The stations with the lowest RMSE values were Dresden and Leipzig (less than 100 [$W \cdot m^{-2}$]). The worst performing station in this regard was the one located in Chemnitz (120.84 [$W \cdot m^{-2}$]).

Table 10. A summary of RMSE for the examined WRF configurations by station [$W \cdot m^{-2}$].

	Dresden	Leipzig	Potsdam	Lindenberg	Goerlitz	Chemnitz
C-ref	109.87	96.45	117.73	112.47	101.32	127.29
C1	85.56	91.26	109.76	107.87	101.32	120.84
C2	86.55	101.07	98.94	101.32	101.32	125.11

Table 11 shows the results of the analysis in the form of MBEs for each station. The C1 and C2 configurations are characterized by overestimated data relative to the values from direct measurements. The average values for the two stations were 5.41 and 9.26 [$W \cdot m^{-2}$], respectively. The C-ref configuration is characterized by the underestimated results of GHI predictions; the average MBE for all stations was -4.56 [$W \cdot m^{-2}$].

Table 11. A summary of MBE for the examined WRF configurations by station [$W \cdot m^{-2}$].

	Dresden	Leipzig	Potsdam	Lindenberg	Goerlitz	Chemnitz
C-ref	-12.62	8.04	-11.51	-3.82	11.05	-18.49
C1	11.04	20.74	-2.77	4.91	11.05	-12.51
C2	16.22	16.13	2.68	11.05	11.05	-1.59

The smallest discrepancies between the obtained MBE values for each station were characterized by the C2 configuration (17.81 [$W \cdot m^{-2}$]), and the largest by C1 (33.25 [$W \cdot m^{-2}$]). The stations with the lowest MBE values (absolute value below 5 [$W \cdot m^{-2}$]) were Potsdam (-3.87 [$W \cdot m^{-2}$]), Lindenberg (4.05 [$W \cdot m^{-2}$]) and Dresden (4.88 [$W \cdot m^{-2}$]). The Leipzig station had the highest MBE values (14.97 [$W \cdot m^{-2}$]).

5. Summary and Conclusions

The analyses conducted showed that irradiance modelling in CEE is achieving increasingly better results, while the complex nephological conditions associated with moving fronts are still the most difficult to model. This article summarizes the results of research into improving the verifiability of short-term solar forecasts made using the WRF model,

specifically for days with cold fronts. For the selected 18 synoptic situations, the Pearson's correlation coefficients ranged from 0.49 to 0.92, depending on the WRF model configuration. These values are slightly higher than those obtained in earlier studies [17]. The dates from the autumn–winter period are characterized by lower values of the indicators RMSE, MAE and MBE. This is certainly related to lower irradiance, which also translates into lower errors. The highest average value of Pearson's correlation coefficient for the analyzed 18 terms associated with moving cold fronts was characterized by the C2 configuration (0.734), while the lowest average was obtained by C-ref (0.707). At the same time, the default configuration was characterized by the largest difference between the minimum and maximum correlation values (0.42), while the C1 and C2 configurations amounted to 0.38 and 0.37, respectively.

This research shows that parameterization of the model, which includes a cumulus parameterization (compared to the default WRF-Solar configuration), improves the quality of the forecasts. The applied modifications to the WRF-Solar model configuration, consisting primarily of activating cumulus parameterization compared to the recommended default configuration, look similar, although they perform better for 5 of the 18 situations associated with cold fronts. Analysis of the remaining six terms showed that the modified configurations perform better for terms with occluded fronts (21 May 2021 and 27 August 2021) by 0.07 and 0.13 (Pearson's coefficient), respectively. Similarly, in the case of RMSE, MAE and MBE, the C1 and C2 configurations had smaller values (in the case of RMSE by more than 27 [$W \cdot m^{-2}$], MAE by more than 15 [$W \cdot m^{-2}$] and MBE by more than 31 [$W \cdot m^{-2}$] than C-ref.

The value of Pearson's correlation coefficient is improved by the parameterizations used in this study, especially for situations associated with passing cold fronts. In the case of forecasts carried out for the reference situations of warm fronts, occluded fronts and high pressure situations, the results obtained by the three configurations of the WRF model were characterized by similar results, both for Pearson's correlation coefficient and the MAE. The proposed configurations of the WRF model (C1 and C2) are characterized by slightly better average values (in total for the 18 terms considered related to the movement of cold fronts) of parameters such as Pearson's correlation coefficient, RMSE and MAE. In contrast, the MBE default configuration is characterized by lower values of 5.56 [$W \cdot m^{-2}$] for C1 and 6.51 [$W \cdot m^{-2}$] for C2.

The analysis of the errors and Pearson's correlation coefficient in the context of the six stations showed that the worst performers were those located in Potsdam and Lindenberg. Such results may be influenced by the surrounding environment, which plays an important role in the hydrological cycle, also influencing the amount of cloudiness in that vicinity, especially for large, but also small, forested areas. The pattern of the influence of forested areas on cloudiness has been extensively described in [64]. The study shows that, especially in the first half of the year, increased cloudiness values are recorded due to the presence of dense forest cover (across Europe).

In conclusion, the main findings from the present research are:

- For cold fronts, the modified parameterizations are characterized by results close to or slightly better than the default configuration;
- For dates with occluded fronts, configurations including the cumulus parameterizations (C1 and C2) are characterized by improved results;
- Among the modified configurations, C1 is characterized by slightly better performance relative to C2, which is expressed, among other things, by smaller discrepancies between maximum and minimum values for the statistics considered.

This investigation shows that changes in parameterization have a positive effect on the achieved forecast results which, in combination with changes in other WRF model settings, e.g., the selection of other static land cover data, can also influence the results of solar forecasts [65]. Further work on forecasts of meteorological elements related to renewable energy sources in the CEE region is crucial for the further development of this energy sector which, in the current economic and political climate, is vitally important. The increasing

number of solar installations will bring even greater challenges for the region's electricity grid managers, which is unavoidable due to existing and future problems with the supply of conventional energy sources (fossil fuels). One of the solutions that can help to solve the existing problems of energy resource management, especially of electricity generated from RES is, among others, forecasts of solar conditions. The character of the region, especially in terms of weather conditions, means that short- and medium-term forecasts are important. Dynamic changes, both in time and space, in meteorological elements mean that especially long-term forecasts, even of basic atmospheric phenomena, are subject to large errors. Based on these, the following recommendations can be made:

- Continued efforts to refine solar irradiance forecasting models, particularly for situations involving moving fronts, can further improve forecast accuracy;
- The use of cumulus parameterization in the WRF-Solar model can lead to better forecast results, especially for days with moving cold fronts;
- Considering the impact of the surrounding environment, including forested areas, on cloudiness can help improve forecast accuracy for these locations;
- Further research should be conducted to better understand the influence of various atmospheric factors on solar irradiance modelling and to implement appropriate parameterizations in forecasting models.

Author Contributions: Conceptualization, M.M.; Methodology, M.M.; Validation, K.K.; Formal analysis, M.M. and A.A.; Investigation, M.M.; Writing—original draft preparation, M.M.; Writing—review and editing, M.M., K.K. and A.A.; Visualization, M.M. and A.A.; Supervision, K.K. All authors have read and agreed to the published version of the manuscript.

Funding: This research was funded by the Military University of Technology in Warsaw, Faculty of Civil Engineering and Geodesy, Institute of Geospatial Engineering and Geodesy statutory research funds UGB/22-816/2023/WAT.

Data Availability Statement: Not applicable.

Acknowledgments: The authors send their special thanks to Wojciech Trzeźniak and Jolanta Siewert for assistance and consultation. The authors acknowledge the DWD Climate Data Center (CDC) for providing the hourly station observation of solar incoming (total/diffuse) and longwave downward radiation for Germany. Numerical simulations were performed using Weather Research and Forecasting Model version 4.3.3 (<https://github.com/wrf-model/WRF/releases>); accessed on 2 June 2022.

Conflicts of Interest: The authors declare no conflict of interest.

References

1. Wolniak, R.; Skotnicka-Zasadzień, B. Development of Photovoltaic Energy in EU Countries as an Alternative to Fossil Fuels. *Energies* **2022**, *15*, 662. [[CrossRef](#)]
2. Hofstätter, M.; Chimani, B.; Lexer, A.; Blöschl, G. A new classification scheme of European cyclone tracks with relevance to precipitation. *Water Resour. Res.* **2016**, *52*, 7086–7104. [[CrossRef](#)]
3. López-Portillo, M.P.; Martínez-Jiménez, G.; Roperio-Moriones, E.; Saavedra-Serrano, M.C. Waste treatments in the European Union: A comparative analysis across its member states. *Heliyon* **2021**, *7*, e08645. [[CrossRef](#)]
4. A European Strategy for Plastics in a Circular Economy. Available online: <https://ec.europa.eu/environment/pdf/circular-economy/plastics-strategy.pdf> (accessed on 15 November 2022).
5. Holz, F.; Von Hirschhausen, C. The Infrastructure Implications of The Energy Transformation in Europe until 2050-Lessons from The EMF28 Modeling Exercise. *Clim. Chang. Econ.* **2013**, *4*, 1340006. [[CrossRef](#)]
6. Share of Energy Consumption from Renewable Sources in Europe. Available online: <https://www.eea.europa.eu/ims/share-of-energy-consumption-from> (accessed on 20 November 2022).
7. Nabi Mughal, S.; Jarial, R.K.; Mughal, S.; Sood, Y.R. A Review on Solar Photovoltaic Technology and Future Trends Condition Monitoring of Power Transformer View project A Review on Solar Photovoltaic Technology and Future Trends. *NCRACIT Int. J. Sci. Res. Comput. Sci. Eng. Inf. Technol.* **2018**, *1*, 227–235.
8. Balthasar, A.; Schreurs, M.A.; Varone, F. Energy Transition in Europe and the United States: Policy Entrepreneurs and Veto Players in Federalist Systems. *J. Environ. Dev.* **2019**, *29*, 3–25. [[CrossRef](#)]
9. Security of Electricity Supply. Available online: https://energy.ec.europa.eu/topics/energy-security/security-electricity-supply_en (accessed on 16 November 2022).

10. Schleich, J. Energy efficient technology adoption in low-income households in the European Union—What is the evidence? *Energy Policy* **2019**, *125*, 196–206. [CrossRef]
11. 2050 Long-Term Strategy. Available online: https://climate.ec.europa.eu/eu-action/climate-strategies-targets/2050-long-term-strategy_en (accessed on 16 November 2022).
12. Gökgöz, F.; Güvercin, M.T. Energy security and renewable energy efficiency in EU. *Renew. Sustain. Energy Rev.* **2018**, *96*, 226–239. [CrossRef]
13. Incecik, S.; Sakarya, S.; Tilev, S.; Kahraman, A.; Aksoy, B.; Caliskan, E.; Topcu, S.; Kahya, C.; Odman, M.T. Evaluation of WRF parameterizations for global horizontal irradiation forecasts: A study for Turkey. *Atmosfera* **2019**, *32*, 143–158. [CrossRef]
14. Lara-Fanego, V.; Ruiz-Arias, J.A.; Pozo-Vázquez, A.D.; Gueymard, C.A.; Tovar-Pescador, J. Evaluation of DNI forecast based on the WRF mesoscale atmospheric model for CPV applications. *AIP Conf. Proc.* **2012**, *1477*, 317. [CrossRef]
15. Isvoranu, D.; Badescu, V. Comparison Between Measurements and WRF Numerical Simulation of Global Solar Irradiation in Romania. *Ann. West Univ. Timis. Phys.* **2013**, *57*, 24–33. [CrossRef]
16. Zempila, M.-M.; Giannaros, T.M.; Bais, A.; Melas, D.; Kazantzidis, A. Evaluation of WRF shortwave radiation parameterizations in predicting Global Horizontal Irradiance in Greece. *Renew. Energy* **2016**, *86*, 831–840. [CrossRef]
17. Mierzwiak, M.; Kroszczyński, K.; Araszkievicz, A. On Solar Radiation Prediction for the East-Central European Region. *Energies* **2022**, *15*, 3153. [CrossRef]
18. Sosa-Tinoco, I.; Prósper, M.A.; Miguez-Macho, G. Development of a solar energy forecasting system for two real solar plants based on WRF Solar with aerosol input and a solar plant model. *Sol. Energy* **2022**, *240*, 329–341. [CrossRef]
19. Skamarock, W.C.; Klemp, J.B.; Dudhia, J.; Gill, D.O.; Liu, Z.; Berner, J.; Wang, W.; Powers, J.G.; Duda, M.G.; Barker, D.M.; et al. A Description of the Advanced Research WRF Model Version 4.3. 2021. Available online: <https://opensky.ucar.edu/islandora/object/opensky:2898> (accessed on 29 June 2023).
20. Powers, J.G.; Klemp, J.B.; Skamarock, W.C.; Davis, C.A.; Dudhia, J.; Gill, D.O.; Coen, J.L.; Gochis, D.J.; Ahmadov, R.; Peckham, S.E.; et al. The Weather Research and Forecasting Model: Overview, System Efforts, and Future Directions. *Bull. Am. Meteorol. Soc.* **2017**, *98*, 1717–1737. [CrossRef]
21. User's Guide for the Advanced Research WRF (ARW) Modeling System. Available online: https://www2.mmm.ucar.edu/wrf/users/docs/user_guide_v4/v4.3/contents.html (accessed on 23 November 2022).
22. Kallio-Myers, V.; Riihelä, A.; Schoenach, D.; Gregow, E.; Carlund, T.; Lindfors, A.V. Comparison of irradiance forecasts from operational NWP model and satellite-based estimates over Fennoscandia Global Horizontal Irradiance (GHI), high latitudes, nowcasting, numerical weather prediction (NWP), satellite-based forecast, solar energy Meteor. *Meteorol. Appl.* **2022**, *29*, e2051. [CrossRef]
23. Martyn, D. *Klimaty Kuli Ziemskiej*; PWN, Wydawnictwo Naukowe: Warsaw, Poland, 1995; ISBN 83-01-11845-8. (In Polish)
24. Perez, R.; Lorenz, E.; Pelland, S.; Beauharnois, M.; Van Knowe, G.; Hemker, K.; Heinemann, D.; Remund, J.; Müller, S.C.; Traunmüller, W.; et al. Comparison of numerical weather prediction solar irradiance forecasts in the US, Canada and Europe. *Sol. Energy* **2013**, *94*, 305–326. [CrossRef]
25. Lamraoui, F.; Booth, J.F.; Naud, C.M. WRF Hindcasts of Cold Front Passages over the ARM Eastern North Atlantic Site: A Sensitivity Study. *Mon. Weather. Rev.* **2018**, *146*, 2417–2432. [CrossRef] [PubMed]
26. Araszkievicz, A.; Kiliszek, D.; Mierzwiak, M.; Da Costa, J.N.; Szołucha, M. GPS-Based Multi-Temporal Variation in Precipitable Water over the Territory of Poland. *Remote Sens.* **2021**, *13*, 2960. [CrossRef]
27. Liu, Q.; Chen, G.; Iwasaki, T. Long-term trends and impacts of polar cold air mass in boreal summer. *Environ. Res. Lett.* **2020**, *15*, 084042. [CrossRef]
28. Sutton, R.T.; Hodson, D.; Mathieu, P.-P. The Role of the Atlantic Ocean in Climate Forecasting. In Proceedings of the ECMWF Workshop on the Role of the Upper Ocean in Medium and Extended Range Forecasting, Shinfield Park, Reading, 13–15 November 2002; Available online: <https://www.ecmwf.int/en/elibrary/76545-role-atlantic-ocean-climate-forecasting> (accessed on 16 June 2023).
29. Ojrzyńska, H.; Błaś, M.; Kryza, M. Precipitable Water Content Climatology over Poland. *Atmosphere* **2022**, *13*, 988. [CrossRef]
30. Salamalikis, V.; Vamvakas, I.; Gueymard, C.A.; Kazantzidis, A. Atmospheric water vapor radiative effects on shortwave radiation under clear skies: A global spatiotemporal analysis. *Atmos. Res.* **2021**, *251*, 105418. [CrossRef]
31. Obregón, M.Á.; Serrano, A.; Costa, M.J.; Silva, A.M. Global Spatial and Temporal Variation of the Combined Effect of Aerosol and Water Vapour on Solar Radiation. *Remote Sens.* **2021**, *13*, 708. [CrossRef]
32. Gueymard, C.A. Impact of on-site atmospheric water vapor estimation methods on the accuracy of local solar irradiance predictions. *Sol. Energy* **2014**, *101*, 74–82. [CrossRef]
33. Bock, O.; Pacione, R.; Ahmed, F.; Araszkievicz, A.; Bałdysz, Z.; Balidakis, K.; Barroso, C.; Bastin, S.; Beirle, S.; Berckmans, J.; et al. Use of GNSS Tropospheric Products for Climate Monitoring (Working Group 3). In *Advanced GNSS Tropospheric Products for Monitoring Severe Weather Events and Climate: COST Action ES1206 Final Action Dissemination Report*; Springer International Publishing: Cham, Switzerland, 2020; pp. 267–402. [CrossRef]
34. Pacione, R.; Araszkievicz, A.; Brockmann, E.; Dousa, J. EPN-Repro2: A reference GNSS tropospheric data set over Europe. *Atmos. Meas. Tech.* **2017**, *10*, 1689–1705. [CrossRef]

35. Baldysz, Z.; Nykiel, G.; Araszkiwicz, A.; Figurski, M.; Szafranek, K. Comparison of GPS tropospheric delays derived from two consecutive EPN reprocessing campaigns from the point of view of climate monitoring. *Atmos. Meas. Tech.* **2016**, *9*, 4861–4877. [CrossRef]
36. Kruczyk, M.; Liwosz, T. Integrated Precipitable Water Vapour Measurements At Polish Polar Station Hornsund From GPS Observations Verified By Aerological Techniques. *Rep. Geod. Geoinform.* **2015**, *98*, 1–17. [CrossRef]
37. Jeworrek, J.; West, G.; Stull, R. Evaluation of Cumulus and Microphysics Parameterizations in WRF across the Convective Gray Zone. *Weather. Forecast.* **2019**, *34*, 1097–1115. [CrossRef]
38. State Aid: Commission Approves Additional German Measures. Available online: https://ec.europa.eu/commission/presscorner/detail/en/IP_22_5811 (accessed on 4 November 2022).
39. Power Producer LEAG Plans €10bn Renewables ‘GigawattFactory’ in Lignite Mining Area. Available online: <https://www.cleanenergywire.org/news/power-producer-leag-plans-eu10bn-renewables-gigawattfactory-lignite-mining-area> (accessed on 9 November 2022).
40. LEAG Errichtet GigawattFactory—Sächsische Agentur Für Strukturentwicklung GmbH. Available online: <https://sas-sachsen.de/leag-errichtet-gigawattfactory-in-der-lausitz/> (accessed on 9 November 2022).
41. Makowski, J. *Geografia Fizyczna Świata*; Wydawnictwo Naukowe PWN: Warszawa, Poland, 2004; ISBN 978-83-01-14218-6.
42. Kondracki, J. Fizycznogeograficzna regionalizacja Niemiec i terenów przyległych w układzie dzisiejszym. *Przegląd Geogr.* **1997**, *LXIX*, 141–148.
43. Public Data of the Institute of Meteorology and Water Management National Research Institute. Available online: <https://danepubliczne.imgw.pl/datastore> (accessed on 15 October 2022).
44. Sykulski, P.; Bielec-Bąkowska, Z. Atmospheric fronts over Poland (2006–2015). *Environ. Socio-Econ. Stud.* **2017**, *5*, 29–39. [CrossRef]
45. What Is a Waving Front?—Met Office. Available online: <https://www.metoffice.gov.uk/weather/learn-about/weather/how-weather-works/waving-front> (accessed on 9 November 2022).
46. Convergence Lines—Met Office. Available online: <https://www.metoffice.gov.uk/weather/learn-about/weather/types-of-weather/clouds/other-clouds/convergence-lines> (accessed on 15 November 2022).
47. Convergence Line—Glossary of Meteorology. Available online: https://glossary.ametsoc.org/wiki/Convergence_line (accessed on 15 November 2022).
48. National Centers for Environmental Prediction/National Weather Service/NOAA/U.S. Department of Commerce. Updated Daily. NCEP GFS 0.25 Degree Global Forecast Grids Historical Archive. Research Data Archive at the National Center for Atmospheric Res. 2015. Available online: <https://rda.ucar.edu/datasets/ds084.1/> (accessed on 2 June 2022).
49. Thompson, G.; Field, P.R.; Rasmussen, R.M.; Hall, W.D. Explicit Forecasts of Winter Precipitation Using an Improved Bulk Microphysics Scheme. Part II: Implementation of a New Snow Parameterization. *Mon. Weather Rev.* **2008**, *136*, 5095–5115. [CrossRef]
50. Nakanishi, M.; Niino, H. An improved Mellor-Yamada Level-3 model: Its numerical stability and application to a regional prediction of advection fog. *Bound. Layer Meteorol.* **2006**, *119*, 397–407. [CrossRef]
51. Nakanishi, M.; Niino, H. Development of an Improved Turbulence Closure Model for the Atmospheric Boundary Layer. *J. Meteorol. Soc. Jpn. Ser. II* **2009**, *87*, 895–912. [CrossRef]
52. Olson, J.B.; Kenyon, J.S.; Angevine, W.A.; Brown, J.M.; Pagowski, M.; Sušelj, K. A Description of the MYNN-EDMF Scheme and the Coupling to Other Components in WRF-ARW. *NOAA Tech. Memo. OAR GSD* **2019**, *61*, 42. [CrossRef]
53. Iacono, M.J.; Delamere, J.S.; Mlawer, E.J.; Shephard, M.W.; Clough, S.A.; Collins, W.D. Radiative forcing by long-lived greenhouse gases: Calculations with the AER radiative transfer models. *J. Geophys. Res. Atmos.* **2008**, *113*, D12. [CrossRef]
54. Jimenez, P.A.; Hacker, J.P.; Dudhia, J.; Haupt, S.E.; Ruiz-Arias, J.A.; Gueymard, C.A.; Thompson, G.; Eidhammer, T.; Deng, A. WRF-SOLAR: Description and clear-sky assessment of an augmented NWP model for solar power prediction. *Bull. Am. Meteorol. Soc.* **2016**, *97*, 1249–1264. [CrossRef]
55. Ruiz-Arias, J.A.; Dudhia, J. A simple parameterization of the short-wave aerosol optical properties for surface direct and diffuse irradiances assessment in a numerical weather model. *Geosci. Model Dev.* **2014**, *7*, 593–629. [CrossRef]
56. Jiménez, P.A.; Dudhia, J.; González-Rouco, J.F.; Navarro, J.; Montávez, J.P.; García-Bustamante, E. A Revised Scheme for the WRF Surface Layer Formulation. *Mon. Weather Rev.* **2012**, *140*, 898–918. [CrossRef]
57. Deng, A.; Gaudet, B.; Duhia, J.; Alapaty, K. Implementation and Evaluation of a New Shallow Convection Scheme in WRF. In Proceedings of the 94th American Meteorological Society Annual Meeting, 26th Conference on Weather Analysis and Forecasting/22nd Conference on Numerical Weather Prediction, Atlanta, GA, USA, 2–6 February 2014.
58. Skamarock, W.C.; Klemp, J.B. A time-split nonhydrostatic atmospheric model for weather research and forecasting applications. *J. Comput. Phys.* **2008**, *227*, 3465–3485. [CrossRef]
59. Jiménez, P.A.; Alessandrini, S.; Haupt, S.E.; Deng, A.; Kosovic, B.; Lee, J.A.; Monache, L.D. The role of unresolved clouds on short-range global horizontal irradiance predictability. *Mon. Weather Rev.* **2016**, *144*, 3099–3107. [CrossRef]
60. DWD Climate Data Center (CDC): Hourly Station Observations of Solar Incoming (Total/Diffuse) and Longwave Downward Radiation for Germany, Version Recent. Available online: https://opendata.dwd.de/climate_environment/CDC/observations_germany/climate/hourly/solar/DESCRIPTION_obsgermany_climate_hourly_solar_en.pdf (accessed on 15 November 2022).
61. Weather Reporting Messages of the World Meteorological Organization, Volume A. CH-1211 Geneva 2, Switzerland. 2012. Available online: https://library.wmo.int/index.php?lvl=notice_display&id=13995 (accessed on 15 November 2022).

62. Wilks, D.S. *Statistical Methods in Atmospheric Sciences*; Kelleher, L., Zaliwa, K., Eds.; Elsevier Inc.: Amsterdam, The Netherlands, 2019; ISBN 9780128158234.
63. Chaturvedi, D.K. Solar Power Forecasting: A Review. *Int. J. Comput. Appl.* **2016**, *145*, 975–8887.
64. Xu, R.; Li, Y.; Teuling, A.J.; Zhao, L.; Spracklen, D.V.; Garcia-Carreras, L.; Meier, R.; Chen, L.; Zheng, Y.; Lin, H.; et al. Contrasting impacts of forests on cloud cover based on satellite observations. *Nat. Commun.* **2022**, *13*, 670. [[CrossRef](#)] [[PubMed](#)]
65. Siewert, J.; Kroszczynski, K. GIS data as a valuable source of information for increasing resolution of the WRF model for warsaw. *Remote Sens.* **2020**, *12*, 1881. [[CrossRef](#)]

Disclaimer/Publisher’s Note: The statements, opinions and data contained in all publications are solely those of the individual author(s) and contributor(s) and not of MDPI and/or the editor(s). MDPI and/or the editor(s) disclaim responsibility for any injury to people or property resulting from any ideas, methods, instructions or products referred to in the content.